

Upper mantle structure of eastern Asia from multimode surface waveform tomography

Keith Priestley,¹ Eric Debayle,² D. McKenzie,¹ and S. Pilidou¹

Received 1 October 2005; revised 8 April 2006; accepted 12 May 2006; published 11 October 2006.

[1] We present a new three-dimensional S_v wave speed and azimuthal anisotropy model for the upper mantle of eastern Asia constrained by the analysis of more than 17,000 vertical component multimode Rayleigh wave seismograms. This data set allows us to build an upper mantle model for Asia with a horizontal resolution of a few hundred kilometers extending to ~ 400 km depth. At 75–100 km depth, there is approximately $\pm 9\%$ wave speed perturbation from the “smoothed PREM” reference model used in our analysis, and the pattern of azimuthal anisotropy is complex. Both the amplitude of the S_v wave speed heterogeneity and the complexity and amplitude of the azimuthal anisotropy decrease with depth. Above ~ 200 km depth the upper mantle structure of the model correlates with surface geology and tectonics; below ~ 200 km depth the structures primarily reflect the advection of material in the upper mantle. Since shear wave speed is principally controlled by temperature rather than by composition, $V_s(z)$ can be used to calculate the temperature $T(z)$, and hence map the lithospheric thickness. We use the relationship of Priestley and McKenzie to produce a contour map of the lithospheric thickness of eastern Asia from the surface wave tomography. This shows an extensive region of thick lithosphere beneath the Siberian Platform and the West Siberian Basin that extends to the European Platform, forming the stable Eurasian craton or core. The eastern portion of the Eurasian craton has controlled the geometry of continental deformation and the distribution of kimberlites in eastern Asia.

Citation: Priestley, K., E. Debayle, D. McKenzie, and S. Pilidou (2006), Upper mantle structure of eastern Asia from multimode surface waveform tomography, *J. Geophys. Res.*, 111, B10304, doi:10.1029/2005JB004082.

1. Introduction

[2] Asia is a mosaic of ancient continental fragments separated by mountain ranges, fold belts, deep sedimentary basins and high plateaus (Figure 1). The region has been shaped by numerous tectonic events, the most recent being the Indo-Asian collision which is responsible for the uplift of the Himalaya Mountains and the Tibetan Plateau, and has induced widespread strain in SE Asia and possibly as far north as Mongolia. The events which formed Asia have left their imprint on the upper mantle structure, and unraveling the tectonic history and understanding the tectonic processes involved in building Asia require a better knowledge of the Asian upper mantle structure. Fundamental mode surface wave studies [e.g., *Ekström et al.*, 1997; *Curtis et al.*, 1998; *Ritzwoller and Levshin*, 1998; *Griot et al.*, 1998a; *Villaseñor et al.*, 2001; *Friederich*, 2003] have furnished a great deal of structural information; however, the inclusion of higher-mode surface waves greatly improves the resolution in the upper mantle because of the independent information they provide to the fundamental mode at shallower

depths and because of the improved sampling they provide over the fundamental mode at deeper depths.

[3] In this paper we focus on the structure of eastern Asia. We use a large, multimode surface wave data set to investigate the S_v wave speed heterogeneity and azimuthal anisotropy of the upper mantle beneath this region on a finer scale than that seen in global tomographic models. We present a high-resolution, three-dimensional (3-D) tomographic image of the Asian upper mantle that displays significant shear velocity features to depths of ~ 200 km, much of which correlates with surface tectonics. Below ~ 200 km depth, the correlation of upper mantle structure with surface tectonics is greatly reduced and is primarily restricted to the subduction zones of the western Pacific.

[4] In our preliminary surface wave tomographic study [Priestley and Debayle, 2003], we compiled a data set of $\sim 13,000$ vertical component Rayleigh wave seismograms from permanent seismographs operating in Eurasia and North America and use these data to determine a 3-D S_v wave speed model for eastern Asia. The data set analyzed in the present study is different from that used by *Priestley and Debayle* [2003]. The new data set we have compiled consists of over 17,000 new measurements using seismograms from both permanent and temporary seismographs in Eurasia, Greenland, and the Canadian Arctic. However, the most important difference between the two studies is not in the increased number of paths but in the fact that the

¹Bullard Laboratories, University of Cambridge, Cambridge, UK.

²Ecole et Observatoire des Sciences de la Terre, Université Louis Pasteur, Strasbourg, France.

TECTONIC PROVINCES OF EASTERN ASIA

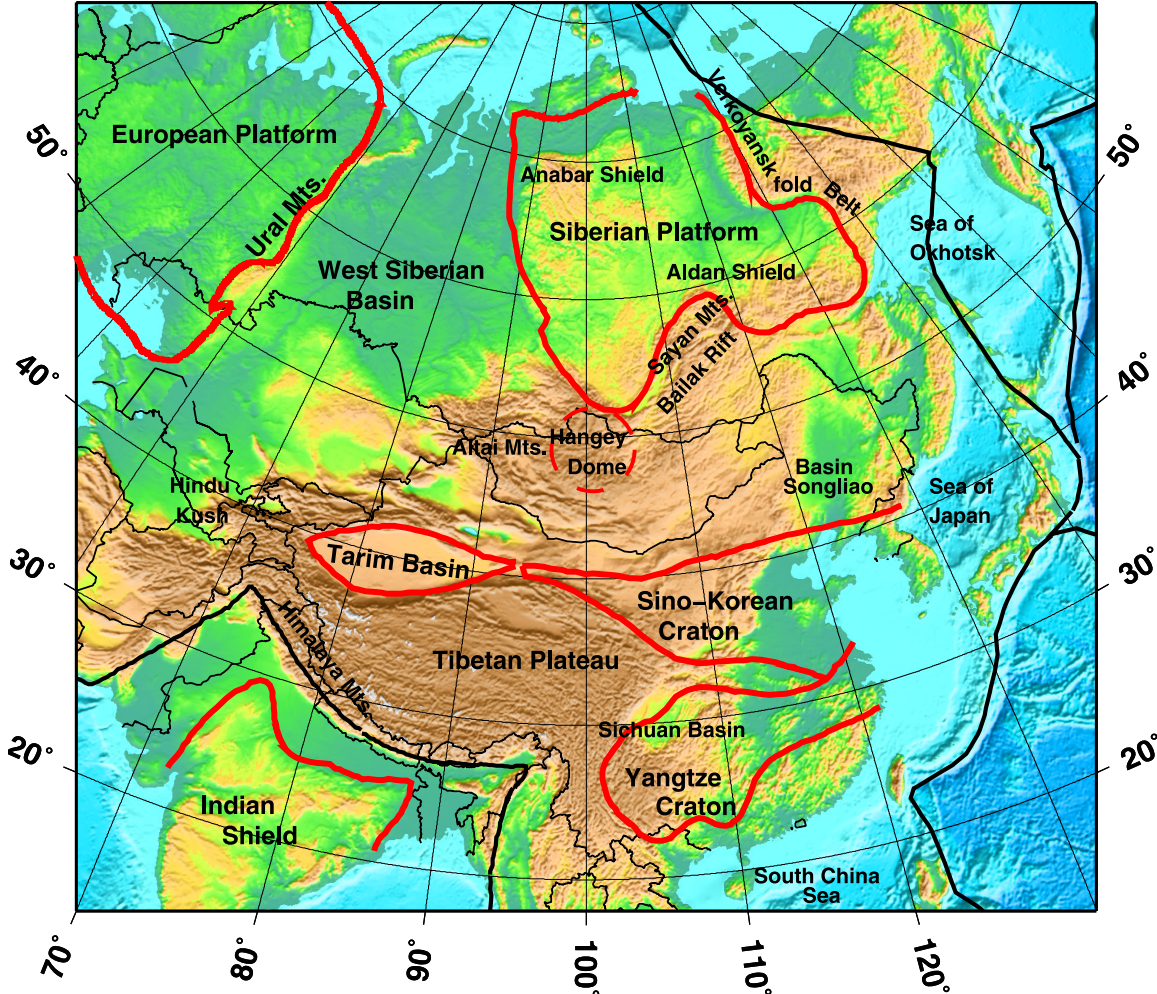


Figure 1. Topographic map of Asia showing the main tectonic features discussed in the text. The boundaries of the European Platform, Siberian Platform, Tarim Basin, Indian Shield, Sino-Korean Craton, and Yangtze Craton are from Goodwin [1991].

propagation path lengths in the present study are short compared with those used by *Priestley and Debayle* [2003]. This feature is crucial when considering the effect of off-great circle propagation. Because of the higher path density, the greater azimuthal cover, the large higher-mode content, and the short path lengths analyzed, this study represents a significant advance in understanding the Asian lithosphere and uppermost mantle.

[5] After summarizing our analysis procedure, we present our east Asian upper mantle model and an assessment of its reliability. We then discuss a number of features of the model in light of the surface geology and tectonics. Finally, we use the relationship between $V_s(z)$ and $T(z)$ of *Priestley and McKenzie* [2006] to derive a model for the thermal lithosphere of eastern Asia. The thermal lithosphere is the cold boundary layer near the Earth's surface in which heat is transported by conduction in contrast to the asthenosphere, where heat is transported by convection. The high-velocity upper mantle lid imaged by seismology is often taken as equivalent to the thermal lithosphere, and the low-velocity zone beneath the lid is taken as equivalent to the astheno-

sphere. However, the mode of heat transport probably has no effect on the seismic velocity, and therefore there is no reason that the thermal lithosphere and the high-velocity lid should be the same.

2. Surface Waveform Fitting and Tomography

[6] We construct the 3-D upper mantle model using the two-stage procedure previously employed in a number of regional-scale surface wave tomography studies [*Debayle and Kennett*, 2000; *Debayle et al.*, 2001; *Priestley and Debayle*, 2003]. In the first stage we use the automated version [*Debayle*, 1999] of the *Cara and Lévéque* [1987] waveform inversion technique in terms of secondary observables for modeling each multimode Rayleigh waveform to determine the path-average mantle S_v wave speed structure. In the second stage we combine the 1-D velocity models in a tomographic inversion [*Montagner*, 1986; *Debayle and Sambridge*, 2004] to obtain the 3-D S_v wave speed structure and the azimuthal anisotropy as a function of depth. This gives a much clearer indication of the

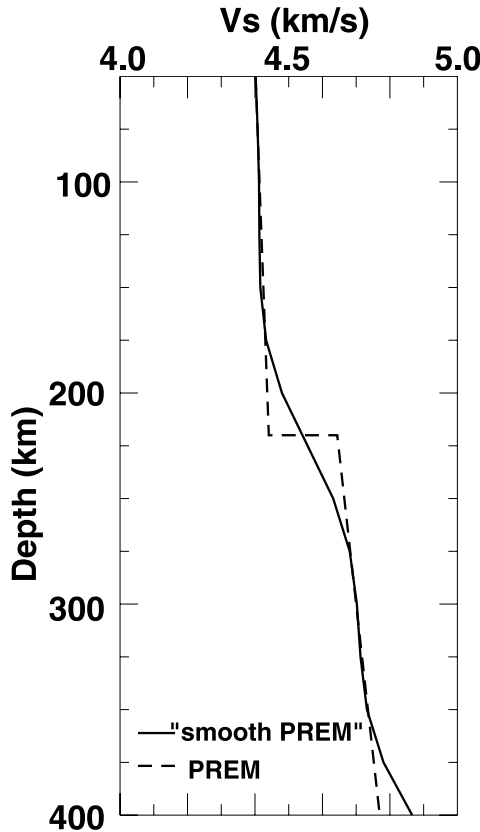


Figure 2. Comparison of PREM [Dziewonski and Anderson, 1981] (dashed line) and the “smooth PREM” (solid line) reference model used in this study.

properties at depth than do group and phase velocity maps which represent a weighted average of the earth structure over a frequency-dependent depth interval.

[7] There are two assumptions inherent in our analysis: that the observed surface waveform can be represented by multimode surface waves, each mode propagating independently, and that they do so along the great circle path. These assumptions are valid for a smoothly varying medium without strong lateral velocity gradients [Woodhouse, 1974] and are widely accepted in surface wave tomography. Kennett [1995] examined the validity of the great circle approximation for surface wave propagation at regional continental scale and concluded that the assumption was valid at longer periods (>50 s) where surface waves cross major structural boundaries such as the continent-ocean transition. Ritzwoller *et al.* [2002] examined the effects of off-great circle propagation and found that for short path lengths (~ 5000 km), the great circle assumption was adequate but led to increasing bias in the inverted model as path length increased. Marquering *et al.* [1996] examined the effect of mode coupling and found that when the analysis was restricted to the fundamental mode and the first few higher modes at relatively low frequencies, the artifacts resulting from neglecting mode coupling were negligible. We therefore restrict our analysis to the fundamental and first four higher Rayleigh mode in the 50–160 s period band, and restrict our analysis to events with

relatively short paths compared to those used in global studies, while maintaining good azimuthal coverage.

[8] Following Kennett [1995], we take a source region specific velocity structure from the 3-D model 3SMAC [Nataf and Ricard, 1996] to improve the source excitation computation and we analyze the seismograms using a modified (smoothed) version of PREM [Dziewonski and Anderson, 1981] for the upper mantle velocity structure (Figure 2) both for the reference model used in extracting the modal information from the seismogram and for the starting inversion and a priori velocity models employed in determining the path-average mantle structure. However, each path has a path-specific crustal model determined by averaging the crustal part of 3SMAC along the path. At 40 s period the maximum sensitivity of even the fundamental mode is located below the crust, so that our data set is primarily sensitive to upper mantle structure, and therefore we assume the crustal structure is known and invert for the upper mantle structure.

3. Data

[9] The distribution of stations and events providing seismograms for this study (Figure 3a) results in excellent density and azimuthal distribution of paths. Most of the earthquakes we study are located on the plate boundaries surrounding Asia. We selected the events from the Harvard centroid moment tensor catalog during the period 1977–2002; however, because of the great expansion of the Global Digital Seismograph Network in the mid-1990s, most of the data are from the period since 1994.

[10] Since the waveforms are automatically fit for each seismogram, the two most important aspects of the analysis are the noise and error detection and the data rejection procedures. For these, we follow the automated procedure described by Debayle [1999], the first step of which is to evaluate the bandwidth over which the seismogram can be analyzed. Debayle and Kennett [2003] compare tomographic results for Australia obtained by inverting the waveforms in the 40–160 s and 50–160 s period bands and found little difference in the deeper part of the model (>130 km) for analysis from either band, but observed that significant disparities could occur at shallower depths. Some of the discrepancy could be attributed to the increased resolution resulting from including the shorter wavelength 40 s period waveforms, but part of the difference probably results from effects such as a departure from ray theory or an inaccurate crustal structure, both of which are more significant at shorter periods. As the Asia region in our study encompasses large variations in crustal thickness, we choose a more restrictive bandwidth criterion than Debayle [1999] and evaluate the signal in the 50, 70, 90, 120, and 160 s period bands.

[11] At each period, the signal-to-noise is deemed adequate if the ratio between the maximum amplitude of the envelope of the signal over the maximum amplitude of the envelope of the noise is greater than 3. From the noise evaluation, the automated waveform inversion chooses the bandwidth for the waveform analysis according to the following sequence of priority: (1) 50, 90 and 160 s; (2) 50, 70 and 120 s; (3) 50 and 90 s; and (4) 50 and 70 s. Once the bandwidth has been chosen, the automated

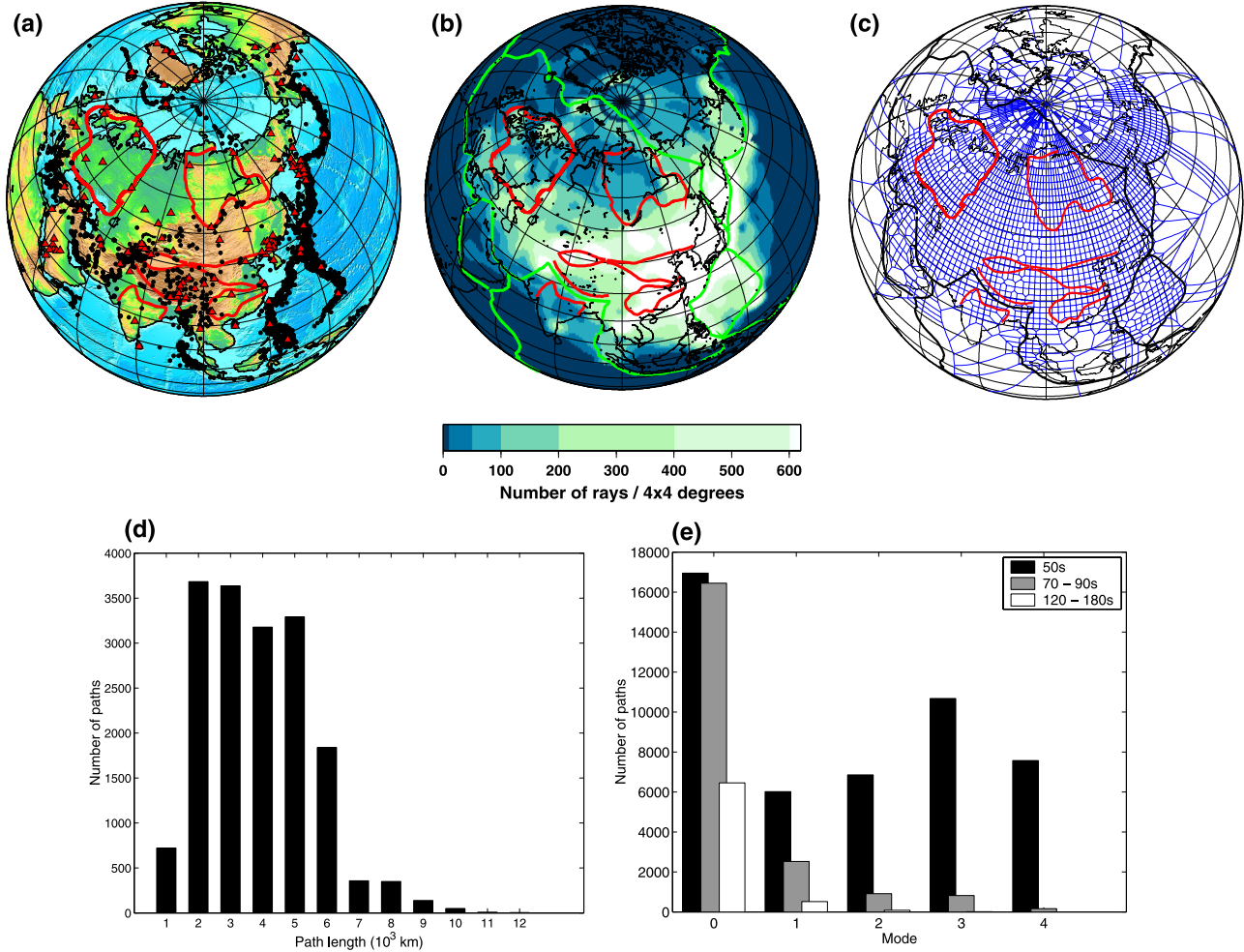


Figure 3. Seismic data and path coverage used in building the east Asia upper mantle model. (a) A total of 17,258 seismograms from 4332 earthquakes (black circles) recorded at 127 seismographs (red triangles). (b) Path density of more than 50 paths per $4^\circ \times 4^\circ$ region over most of Asia. (c) Achieved Voronoi diagram for the data path coverage. For most of Asia, $2^\circ \times 2^\circ$ coverage is achieved. (d) Path length distribution of the data. The average path length is 4011 km. (e) Modal and frequency distribution of the data.

waveform analysis is performed according to the procedure and criterion described by *Debayle* [1999]. The inversion is considered successful if the final model provides a good fit to both the secondary observables and the observed seismogram and if the inversion has converged toward a unique and stable velocity model.

[12] This extremely conservative procedure was used to assemble a data set of 17,258 1-D path average Earth velocity models from which we construct the 3-D velocity and azimuthal anisotropy model. Figure 3b shows that a density of more than 50 paths per $4^\circ \times 4^\circ$ cell is achieved throughout Asia and more than 300 paths per $4^\circ \times 4^\circ$ cell is achieved over most of east Asia. In Figure 3c we use a Voronoi diagram [*Debayle and Sambridge*, 2004] to describe the azimuthal distribution of the path coverage. Each Voronoi cell gives the smallest region with a sufficient azimuthal distribution of paths to geometrically resolve the azimuthal anisotropy [*Debayle and Sambridge*, 2004]. Over most of Asia we achieve a cell size of 2° by 2°

(Figure 3c). Figure 3d shows the path length distribution. Only a small fraction of our paths exceeds 6000 km and the average path length is 4011 km. All paths are greater than 1000 km to avoid finite source effects. Figure 3e shows the frequency and modal composition of the data. While much of our data set consists of fundamental mode measurements, there is a significant higher-mode content in the data set.

4. Tomographic Maps

[13] The S_v wave speed heterogeneity and azimuthal anisotropy maps for our eastern Asia model are shown in Figure 4. The lateral smoothing in the tomographic inversion is controlled using a Gaussian a priori covariance function defined by a scale length L_{corr} and a standard deviation σ . L_{corr} defines the distance to which adjacent points of the model are correlated and acts as a spatial filter; σ controls the amplitude of the perturbation in Earth structure allowed (velocity perturbation, azimuthal anisotropy).

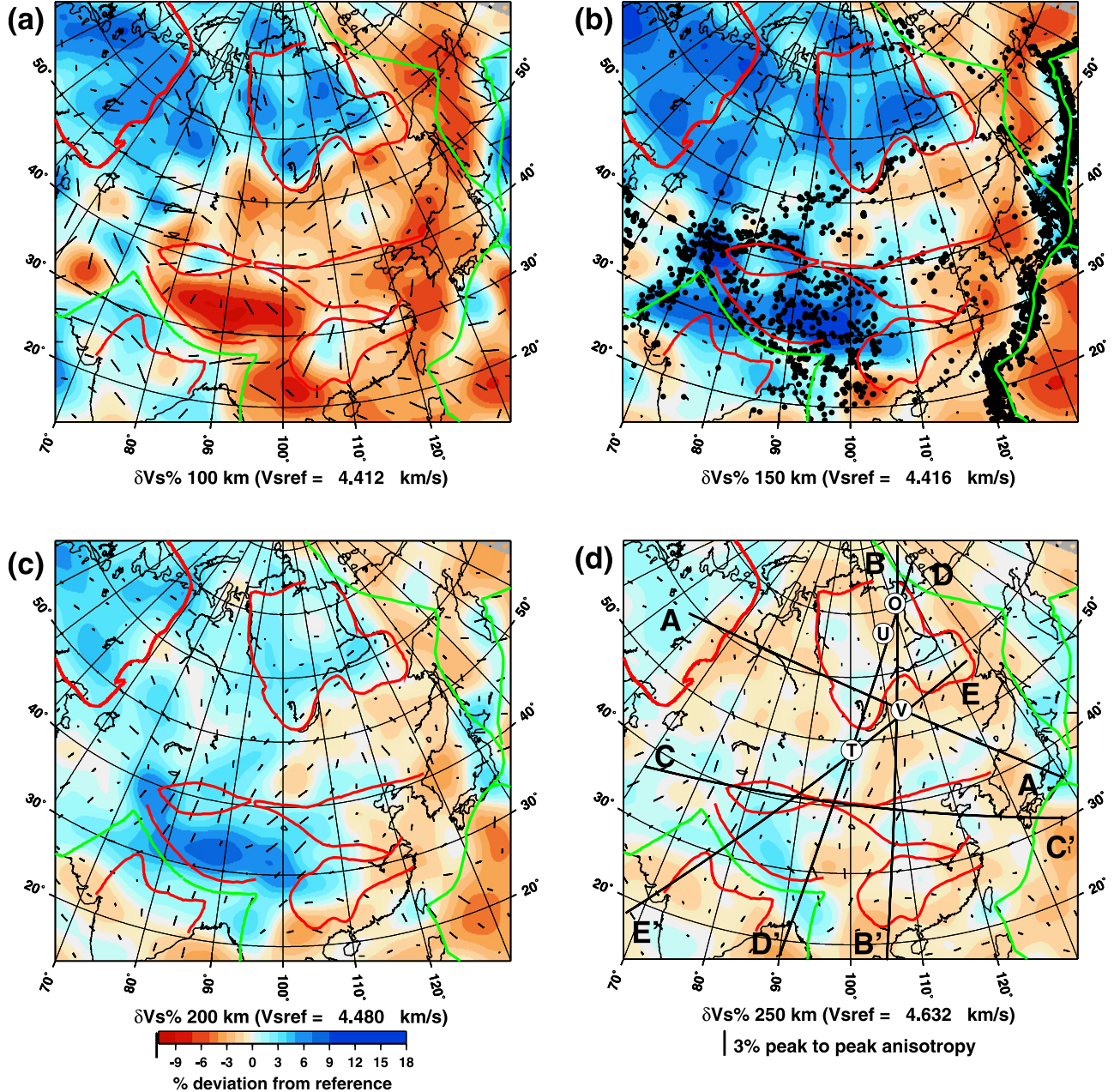


Figure 4. Depth sections through the model are shown at (a) 100 km, (b) 150 km, (c) 200 km and (d) 250 km depth. Each of the depth sections has the reference model velocity ($V_{s\text{ref}}$) at the depth indicated beneath the map. The percentage deviation from the reference velocity is denoted by the scale below the 200 km depth map in Figure 4c. The short black lines on the maps denote the fast direction of the horizontally propagating S_v waves. The bar length for 3% peak-to-peak anisotropy is shown below the 250 km depth map in Figure 4d. Red contours denote tectonic features from Figure 1; green lines denote plate boundaries. Magnitude 5 and greater earthquakes with well-constrained depths from the Engdahl-Van der Hilst-Buland (EHB) catalog [Engdahl *et al.*, 1998] are plotted on Figure 4b; the locations of the five profiles shown in Figure 8 are indicated in Figure 4d. The symbols O, U, V, and T on Figure 4d denote the locations of the kimberlite volcanic sites whose upper mantle nodule analysis is discussed in the text and are used to constrain the mantle geotherms shown in Figure 10.

ropy, or both) in the inversion. The model shown in Figure 4 was obtained using $L_{\text{corr}} = 400$ km for both velocity heterogeneity and azimuthal anisotropy, $\sigma = 0.05 \text{ km s}^{-1}$ for the velocity perturbation and $\sigma = 0.003 \text{ km s}^{-1}$ for the azimuthal anisotropy variation. This choice favors a smooth

model, considering our shortest wavelengths (about 200 km at 50 s period) and dense path coverage.

[14] The correlation of mantle features with known mantle structure (e.g., subducted slabs) and surface features and the tests discussed below show that these values for L_{corr}

and σ and the path density (Figure 3b) enable us to resolve structures with horizontal wavelengths of a few hundred kilometers for the uppermost ~ 400 km of the model. Although the lateral resolution that can be achieved in surface wave inversion with ray theory is debated [Yoshizawa and Kennett, 2002; Spetzler and Snieder, 2001], recent studies suggest that the shortcomings of ray theory compared to a more sophisticated finite frequency theory can be counterbalanced by the choice of the regularization of the inversion [Sieminski et al., 2004; Trampert and Spetzler, 2006]. In the present study, we use a scheme for the tomographic inversion which facilitates the choice of a physically based regularization, because the prior information imposed on the inverse problem through the parameters L_{corr} and σ has a direct interpretation in terms of the physical properties of the model [Debayle and Sambridge, 2004]. Sieminski et al. [2004] show that with such a physically based regularization of the inverse problem and using a dense path coverage, it is possible to offset the shortcomings of ray theory and to detect heterogeneities with length scales smaller than the wavelength of the data set. This likely explains why structures with a small horizontal extension such as slabs are detected in this study.

[15] In this paper, we do not discuss the details of the anisotropic directions at lithospheric depths. Within the lithosphere, the complex tectonic history of Asia may have produced anisotropic patterns with directions changing over horizontal wavelength smaller than our lateral resolution, a situation where our tomographic approach does not allow us to reliably recover the anisotropic direction. We are more likely to recover properly the anisotropy in the asthenosphere, where large scale patterns may control its organization. However, the azimuthal anisotropy signal is weak below the lithosphere as discussed in section 7.

[16] At 75–100 km depth there is approximately $\pm 9\%$ wave speed perturbation from the reference model and the pattern of azimuthal anisotropy is complex. Both the amplitude of the S_v wave speed heterogeneity and the complexity and amplitude of the azimuthal anisotropy decrease at deeper depths. Above ~ 200 km depth the upper mantle structure of the model is correlated with surface geology and tectonics; below ~ 200 km depth the structures primarily reflect the advection of material in the upper mantle. The main features of our model are as follows:

[17] 1. Pronounced low wave speeds exist beneath the back-arc basins of the western Pacific subduction zones off the coast of eastern Asia and high wave speeds exist along narrow, elongated zones corresponding to the location of the subducted oceanic lithosphere beneath Kamchatka, the Kuriles, Japan, Taiwan, and the Philippines.

[18] 2. Low wave speeds exist at shallow depths (75–100 km) beneath Tibet but at deeper depths (150–200 km) the mantle beneath the whole of Tibet is fast with respect to the reference model. The high wave speed mantle at these depths beneath Tibet merges to the south with high wave speeds beneath India and to the east with high wave speeds beneath southeastern China. From 250 km to the bottom of the model, high wave speeds persist beneath southern Tibet.

[19] 3. High wave speed upper mantle exists beneath the cratons to 200–225 km depth, but at greater depth, the wave speeds beneath the cratons are close to that of the reference model.

[20] We elaborate on the model features below but first discuss the reliability and resolution of the upper mantle model.

5. Reliability of the 3-D Model

[21] There are a number of factors in both stages of the analysis which influence the reliability of the model. In addition to the great circle propagation approximation and the neglect of mode coupling discussed above, the model reliability is affected by the choice of reference model, path coverage, and poor knowledge of the uninverted parameters.

[22] Cara and Lévéque [1987] show that for their waveform inversion technique used in stage one of our analysis, the final velocity structure is weakly dependent on the reference model. However, errors in uninverted parameters such as earthquake source parameters and crustal structure will cause errors in the 1-D path average velocity models determined in the first stage of the analysis. Ritzwoller and Levshin [1998] and Maggi and Priestley [2005] examined the effect of a systematic shift in event locations on regional-scale surface wave tomography and found that if the path density and azimuthal coverage are good, as they are in this study, the effects of the mislocation were restricted to the source region and were of small magnitude. Errors in the assumed crustal structure will influence the shallow mantle structure. Debayle and Kennett [2000] show that reasonable errors in crustal thickness have little effect on the mantle structure below 100–125 km depth. In addition, we have tested a subset of our data using the CRUST2 [<http://mahi.ucsd.edu/Gabi/rem.dir/crust/crust2.html>] model in place of the 3SMAC crustal model and found little difference in the upper mantle structure. Differences in mantle structure resulting from the choice of crustal models are discussed in greater detail by Pilidou et al. [2005].

[23] The resolution achieved and the presence of artifacts in the 3-D model determined in the second stage of the analysis are primarily the result of the path coverage, and the frequency and modal makeup of the surface waves. The continuous regionalization approach we use to determine the tomographic model provides an a posteriori error estimate for the extracted model, and this is a useful guide to the resolution attainable from the data. It is well known that in regions where resolution is weak, the a posteriori error nearly equals the a priori error [Tarantola and Valette, 1982]. As a result of the dense path coverage and rich higher-mode content of the data set, the a posteriori error (Figure 5) is low ($<0.035 \text{ km s}^{-1}$) over most of Asia to 400 km depth compared to the a priori error (set to 0.05 km s^{-1}). The a posteriori error maps (Figure 5) display a pattern similar to the path distribution (Figure 3b) and optimum Voronoi (Figure 3c) diagram.

[24] We also use a traditional checkerboard test to evaluate how well the 3-D tomographic images reflect the shapes and amplitudes of a given distribution of shear velocity heterogeneity. For this test we first create an input model consisting of $1000 \text{ km} \times 1000 \text{ km} \times 100 \text{ km}$ thick blocks having a $\pm 6\%$ alternating wave speed variation superimposed on smooth PREM. We calculate synthetic multimode seismograms for the same source parameters,

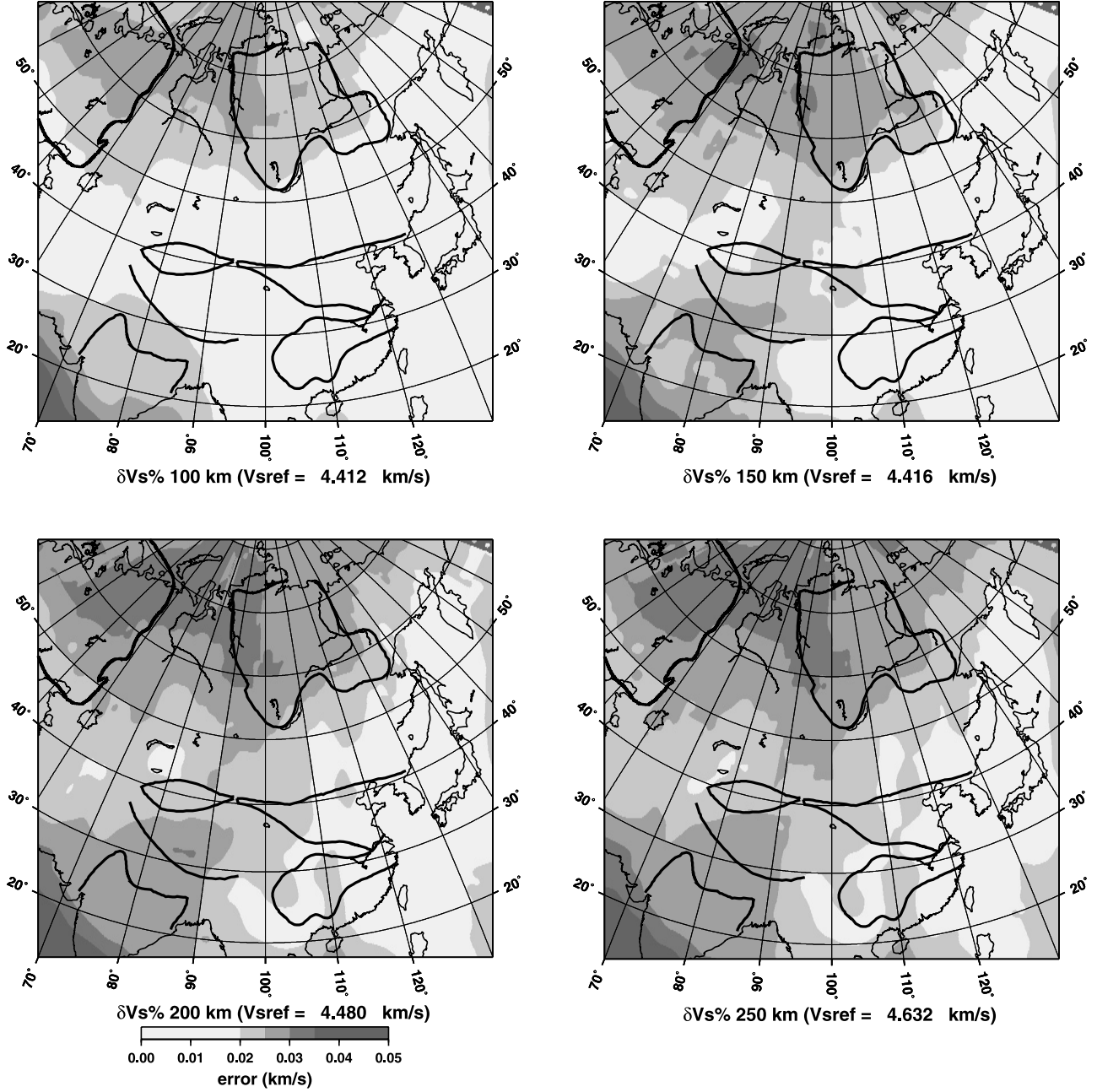


Figure 5. A posteriori error for the model at four depths.

frequency content, modal distribution, and event-receiver combinations as in the observed data. The synthetic seismograms are then inverted in exactly the same way as the real data using the automated procedure outlined in section 2. By starting with the initial step of the 1-D waveform inversions, our tests not only provide insights on the spatial resolution of the model attained from the path coverage, but they also yield information on the depth resolution attained from the frequency and modal content of the seismograms analyzed. Figure 6 shows slices through the recovered checkerboard model at depths between 75 and 350 km. The geometry of the input model (Figure 7) is retrieved over the whole depth range except at the edges of the maps, and there is little indication of horizontal smearing. At shallow depths the amplitude of the input model is faithfully

recovered. At 250 km depth the amplitude recovery is $\sim 50\%$ of the input amplitude, and by 350 km depth the amplitude recovery has dropped to $\sim 25\%$ of the input amplitude.

[25] The final test evaluates the azimuthal anisotropy resolution of the models (Figure 7). To the checkerboard model described above we add a pattern of azimuthal anisotropy with a peak-to-peak amplitude of 5% with a pattern for the fast anisotropy that displays an abrupt change in direction (Figure 7a). The magnitude and direction of the anisotropy pattern are in general well recovered (Figure 7b) in areas of good azimuthal coverage (Figure 3c). In the region of abrupt change in anisotropic direction, the horizontal smoothing introduced in the inversion and by the long-period surface waves can, however, produce a local

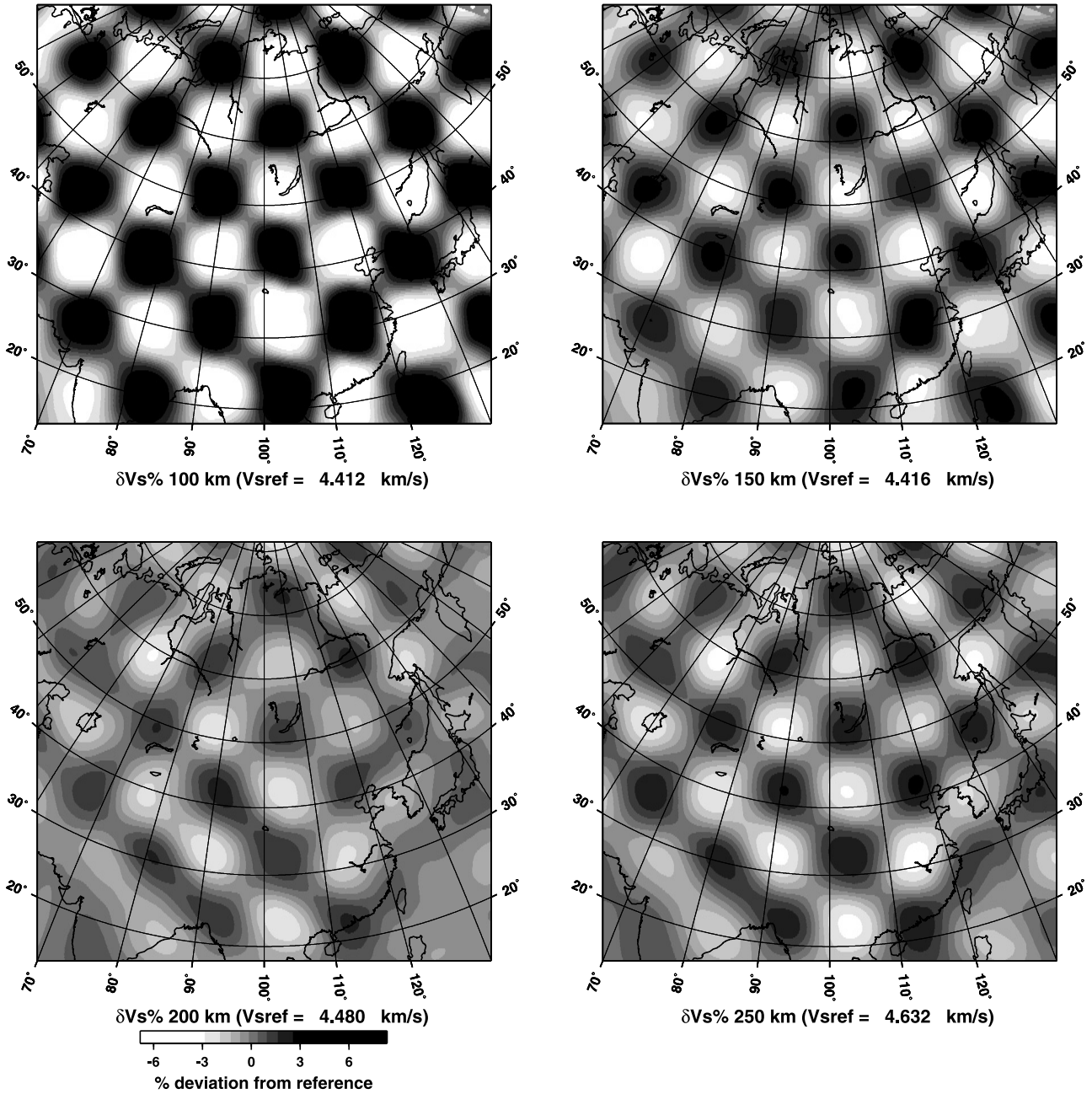


Figure 6. Checkerboard resolution test for the model at the four depths. Blocks of the input synthetic model are 1000×1000 km in lateral dimension and 100 km thick. The input model at 100 km depth is shown in Figure 7.

anisotropic pattern that is wrong in both amplitude and direction. Thus the anisotropic pattern obtained with surface waves is likely to be meaningful only where the anisotropy varies slowly with respect to the horizontal resolution of the surface waves. It may be that such regions are not common within the continental lithosphere where anisotropy generally reflects the complex tectonic history. In regions where abrupt changes in anisotropic direction are present or where variations in anisotropic direction occur over distances smaller than the horizontal resolution, the horizontal smoothing of the surface waves will not allow recovery of the azimuthal anisotropy directions. For this reason, we will discuss only the general trend of the anisotropy and not the

fine details. In more extensive azimuthal anisotropy tests we found a coupling between azimuthal anisotropy and lateral heterogeneity with as much as 1–2% lateral heterogeneity arising from the azimuthal anisotropy [Pilidou et al., 2005]. We have conducted similar tests with our Asia data set and find similar levels of coupling.

6. Discussion

[26] Asia is made up of continental and oceanic fragments accreted to the southern margin of stable Eurasia consisting of the Siberian Platform and the West Siberian Basin [Sengor and Natal'in, 1996; Yin and Nie, 1996]. The main

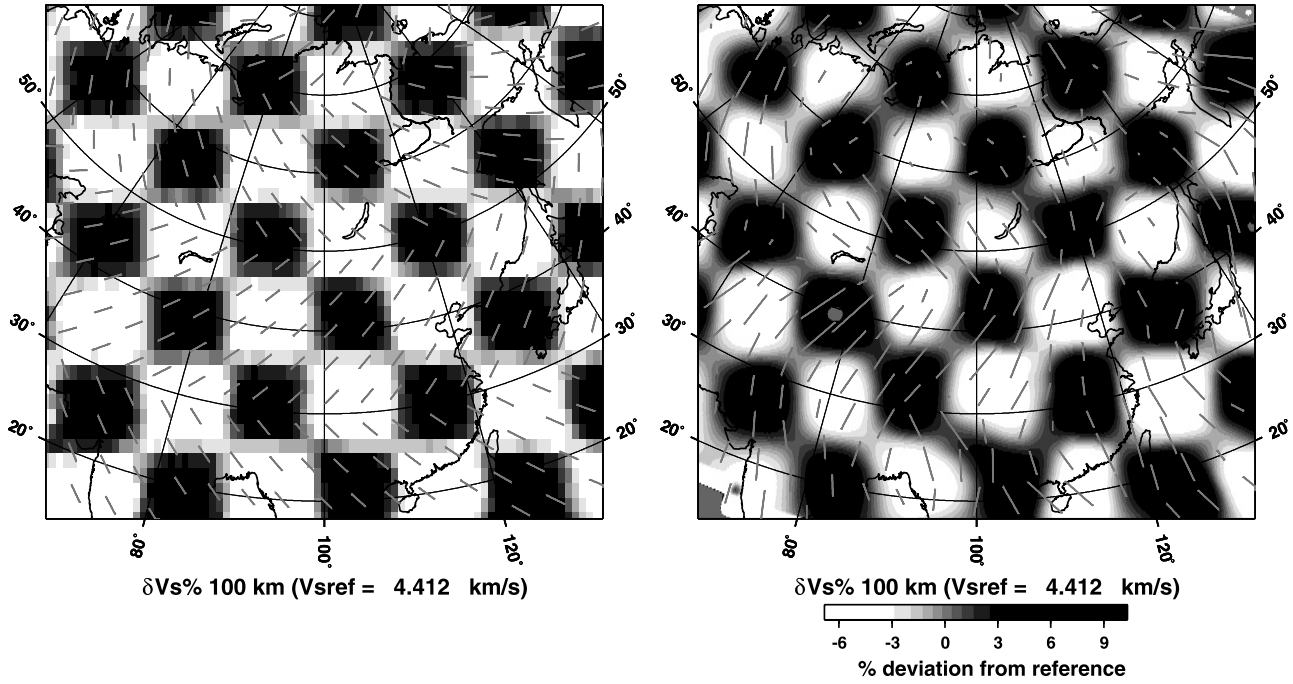


Figure 7. (a) Input synthetic model at 100 km depth for the azimuthal anisotropy test and (b) output model from the inversion at 100 km depth.

accreted fragments include the north China block or Sino-Korean craton, the south China block or Yangtze craton, and India. These and other smaller blocks are separated by sutures whose geometries have been significantly modified at various stages by later collisional and translational events. At present, compressional tectonics dominates most of central Asia while extensional tectonics dominates most of eastern China. There is a corresponding difference in our upper mantle model where areas primarily under compression are underlain to ~ 200 km depth with high wave speeds relative to the reference model, and areas primarily under tension are underlain by low wave speed upper mantle to ~ 200 km depth relative to the reference model (Figure 4). Deeper structures seen in the model are associated with the advection of material in the upper mantle, particularly the subduction zones in the western Pacific.

6.1. Stable Eurasia

[27] The Siberian Platform (Figure 1) forms the eastern-most part of stable Eurasia. The Platform is mostly covered by 2–14 km of Proterozoic-to-Cretaceous sediments [Griffin et al., 1999] and the 250 Ma flood basalts of the Siberian traps [Zolutkin and Al'mukhametov, 1988], but its Archean basement outcrops in the Aldan Shield in the southeast and Anabar Shield in the north. The Siberian Platform is bordered to the south and east by Phanerozoic fold-and-thrust belts formed during the assembly of Pangea [Mitrofanov and Taskin, 1994; Griffin et al., 1999]. Crustal evolution of the platform may have begun as early as 3.5 Ga, but the oldest rocks found thus far are ~ 3.3 Ga [Jahn et al., 1998].

[28] The Siberian Platform is well delineated in our upper mantle S_v model. Between 100 and 200 km depth (Figures 4a–4c) the boundary of the high wave speed root beneath the eastern part of the Siberian Platform closely

matches the geologically mapped boundary corresponding to the western boundary of the Verkhoyansk fold-and-thrust belt at the surface. However, in the west, the high velocity upper mantle lid extends across the West Siberian Basin as far as the Ural Mountains where it merges with the high velocity root beneath the East European Platform (Figures 4a–4c and 8a). At 250 km depth the velocity beneath both the Siberian Platform and the West Siberian Basin is close to that of the reference model (Figures 4d, 8a, 8b, and 8d). The checkerboard tests (Figures 9a, 9b, and 9d) show that the depth resolution in this part of the model is excellent.

[29] The Baikal rift (discussed in more detail below) at the southern boundary of the Siberian Platform occurs above a sharp transition in the S_v model between the high velocities beneath the platform and the low velocities beneath the central Asian fold belt (Figures 4a–4c, 8a, and 8b). However, to the northeast of Lake Baikal, the high-velocity root of the Siberian Platform extends somewhat further south from the location of the mapped boundary at the surface (Figures 4a–4c and 8b). The seismicity northeast of Lake Baikal follows more closely the boundary of the Siberian Platform seen in the tomographic model than it does the mapped boundary of the platform at the surface (Figure 4b). The right stepping en echelon basins of the Baikal rift northeast of the lake also follow this trend [Logatchev, 1993] suggesting that the strong, cold mantle root of the Siberian Platform is controlling the location of the rift. The mismatch between the surface manifestation of the Siberian Platform and the southern boundary of its upper mantle root probably results from the thrusting from the south of the Sayan Mountains over the platform basement [Mitrofanov and Taskin, 1994].

[30] The 200–225 km values we find for the thickness of the high velocity lid beneath the Siberian Platform

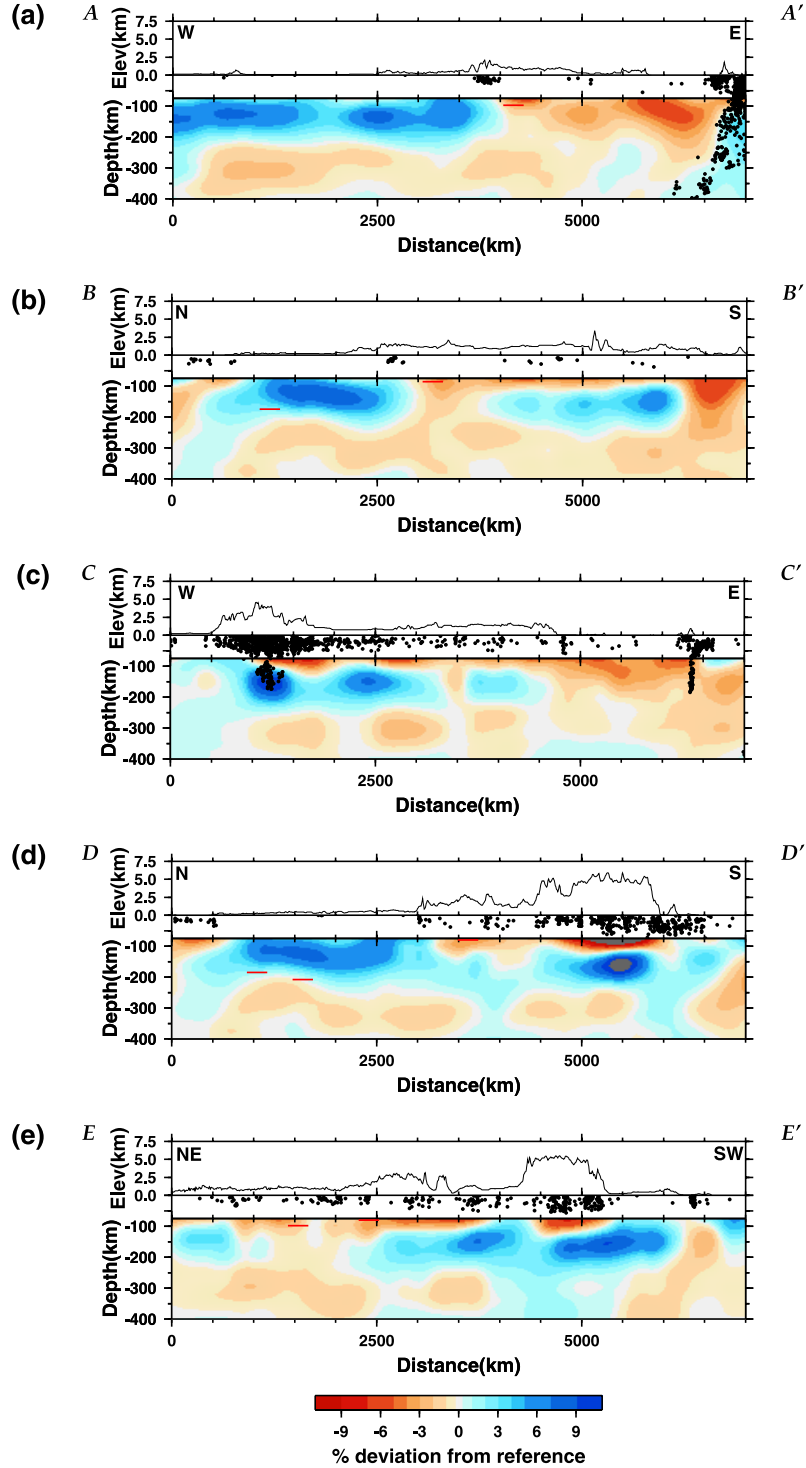


Figure 8. Five profiles showing the depth variation of the S_v wave speed heterogeneity. Each profile is 7000 km long and the locations of the profiles are denoted on Figure 4d. The S_v wave speed heterogeneity is only plotted below 75 km depth. Black dots are magnitude 5 and greater earthquakes with well-constrained depths from the EHB catalog [Engdahl et al., 1998], projected onto the profile. The profile topography is plotted above. Note the difference in depth and elevation scales. The short red lines on the cross sections denote the lithospheric thickness from the four sites of Figure 10. The error distribution and checkerboard test results for the profiles are shown in Figure 9.

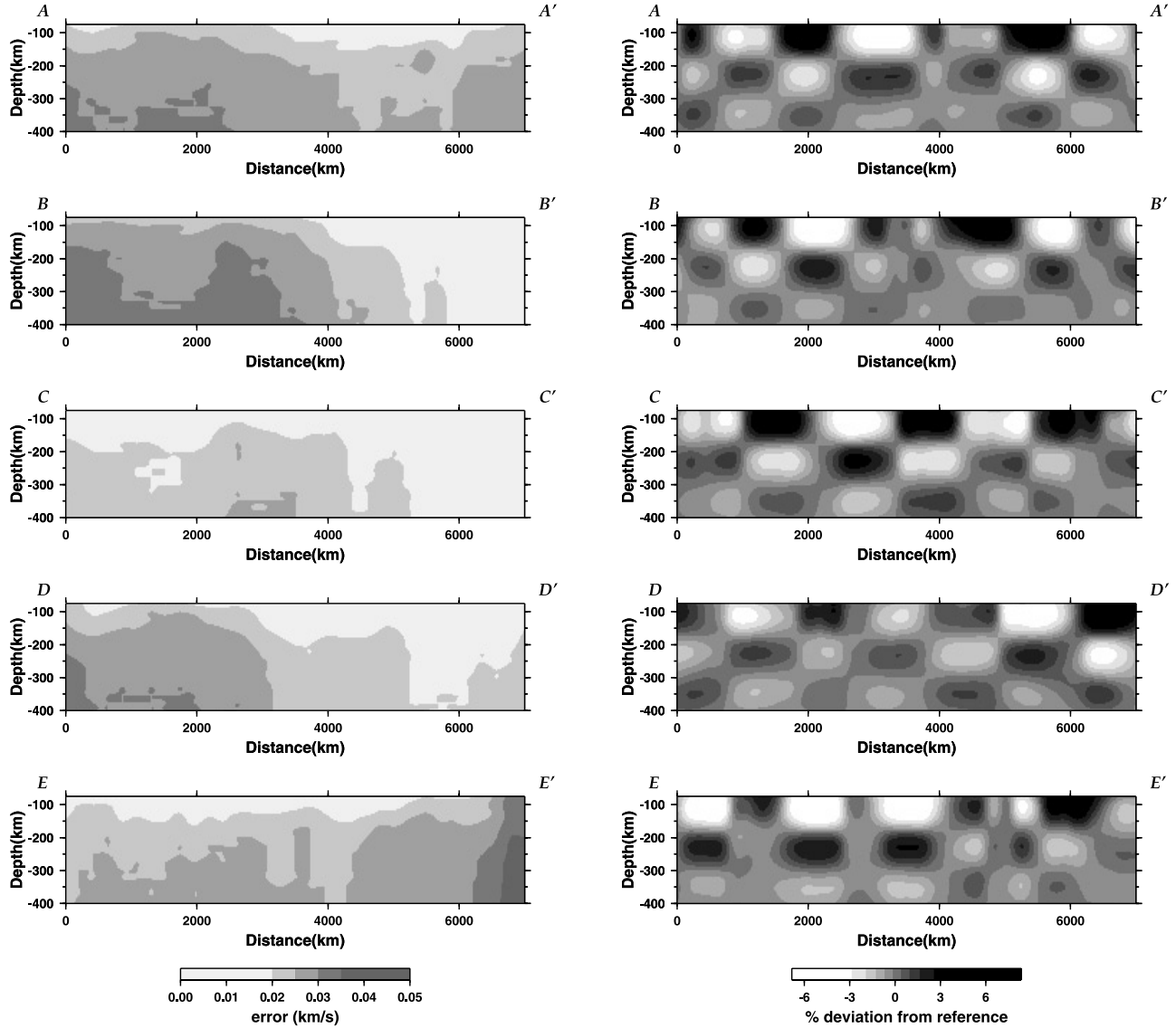


Figure 9. A posteriori error and checkerboard resolution test for the five profiles shown in Figure 8. The a posteriori error is less than 0.035 km s^{-1} over most of the profiles. The checkerboard plots shown are for the full synthetic waveform test and show that the horizontal smearing is minimal and that the vertical resolution is about 25 km.

(Figures 4, 8a, 8b, and 8d) differ significantly from the values of the thermal lithospheric thickness of 350 km or more determined by Artemieva and Mooney [2001]. However, their thermal lithospheric model of the Siberian Platform is based on rather sparse heat flow data and assumptions about the radioactive heat production of the crust.

[31] The thickness of the thermal lithosphere can be determined directly from the upper mantle nodules brought to the surface in some volcanic eruptions. There are two sites on the Siberian Platform where kimberlite eruptions have brought up mantle nodules: Udachnaya and Obnazhennaya (Figure 4d), and the mineralogy of such nodules can be used to estimate the pressure and temperature at which they last equilibrated. We use the Brey and Kohler [1990] expression for the solubility of aluminum in enstatite in the presence of garnet to estimate the pressure (depth)

and the Brey and Kohler [1990] expression for the inter-solubility of enstatite and diopside to obtain the temperature. The steady state temperature within the lithosphere was calculated using the expressions in McKenzie *et al.* [2005]. For this calculation the 40 km thick crust [Suvorov *et al.*, 2002; Pavlenkova *et al.*, 2002] is divided into two layers, both with the same thermal conductivity, $2.5 \text{ W K}^{-1} \text{ m}^{-1}$. The heat generation rate for the upper crust is $1.12 \mu \text{W m}^{-3}$ and the lower crust is $0.4 \mu \text{W m}^{-3}$, values suggested by Jaupart and Mareschal [1999] for granulite. The thicknesses of the upper and lower crust were varied to fit the pressure and temperature estimates from the nodules while keeping the total crustal thickness equal to 40 km. The heat generation in the mantle portion of the mechanical boundary layer (MBL) is taken to be zero and the thermal conductivity is taken to be a function of temperature [Schatz and Simmons, 1972; Hofmeister, 1999;

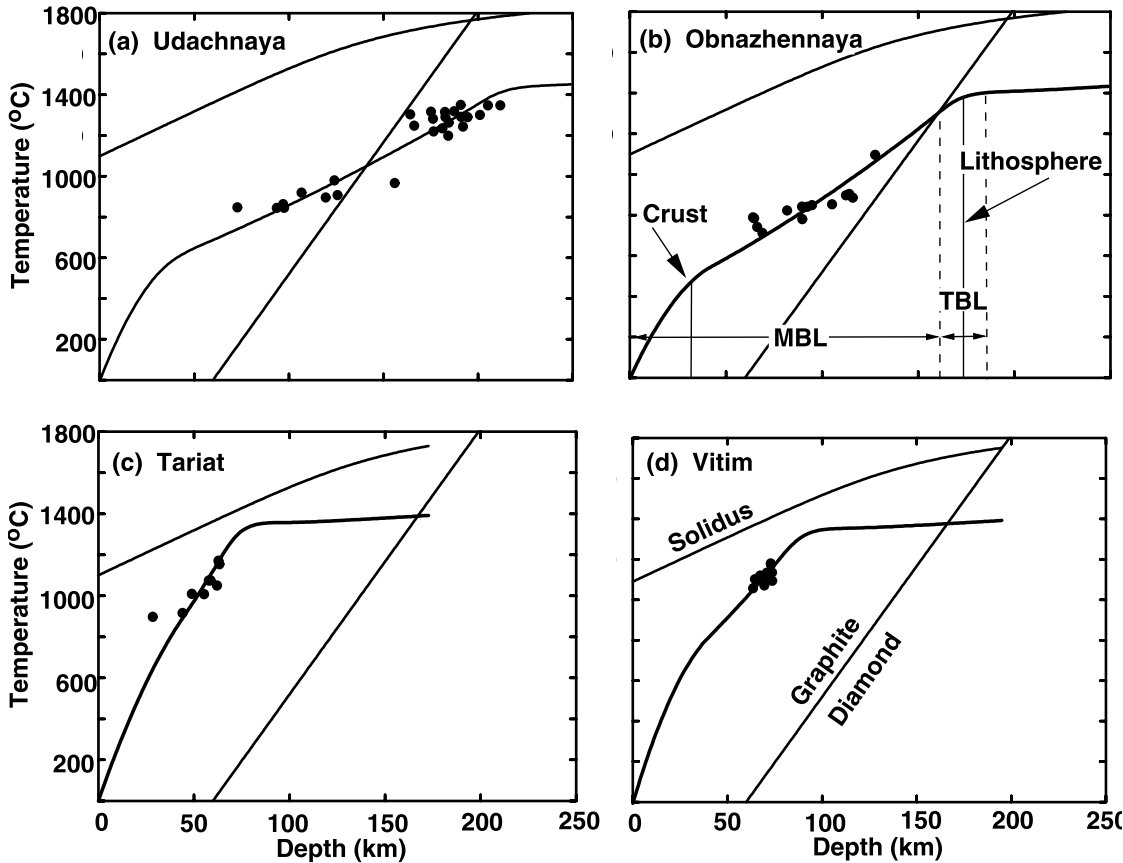


Figure 10. Geotherms fit to the temperature and pressure (depth) estimates from the upper mantle volcanic nodules for the four sites denoted in Figure 4: (a) Udachnaya (U), (b) Obnazhennaya (O), (c) Tariat (T), and (d) Vitim (V). The sources of the nodule data are *Boyd et al.* [1997] for Udachnaya, *Taylor et al.* [2003] for Obnazhennaya, *Ionov et al.* [1993] for Tariat, and *Kopylova et al.* [1995] for Vitim. The annotations on Figure 10b show the mechanical boundary layer (MBL), the thermal boundary layer (TBL), the crust, and the lithosphere [McKenzie et al., 2005], and on Figure 10d show the solidus [McKenzie and Bickle, 1988] and the graphite-diamond transition [Kennedy and Kennedy, 1976]. Udachnaya and Obnazhennaya are located on the Siberian Platform and have considerably thicker thermal lithosphere than do Tariat and Vitim which are located in the orogenic belt south of the Siberian Platform.

Xu et al., 2004]. At the base of the MBL the heat flux and temperature must be the same as those at the top of the thermal boundary layer (TBL). The temperature structure within the TBL was obtained from the expressions given by Richter and McKenzie [1981] and with an interior potential temperature of 1315°C.

[32] Figures 10a and 10b show the best fitting geotherm to the nodule data from Udachnaya and Obnazhennaya calculated using this method. The lithospheric thickness is the intersection of the conductive and convective geotherms in the absence of the thermal boundary layer. The resulting thickness of the thermal lithosphere is 215 km at Udachnaya and 173 km at Obnazhennaya. The uncertainty in the mean thickness of the lithosphere beneath these two sites is probably about ± 25 km [Priestley and McKenzie, 2006]. Figures 10c and 10d show the geotherm determined from analysis of nodules from the Tariat and Vitim volcanics (Figure 4). The thermal lithosphere at these sites south of the Siberian Platform is 79 and 93 km, respectively, consistent with the absence of the high-velocity lid to the south of the Siberian Platform seen in the tomographic

model (Figures 4a–4c, 8a, 8b, 8d, and 8e). The lithospheric depths determined from the nodules in Figure 10 are also plotted in Figure 8. The transition from high velocities to low velocities relative to the reference model occurs near the depth where the temperature gradient decreases sharply at the base of the thermal lithosphere. The geotherms in Figure 10 show a marked difference between the thermal lithosphere beneath the platform and the younger orogenic belts, consistent with the seismic results. At depths shallower than ~ 175 km, the upper mantle of the platform is considerably colder and has a higher wave speed structure than does the upper mantle beneath the Paleozoic fold belts.

6.2. Eastern China

[33] Eastern China consists of a number of Precambrian blocks surrounded by Phanerozoic fold belts [Li, 1994; Li et al., 1995] (Figure 1). The Sino-Korean Craton lies south of the Siberian Platform and is separated from it by the Paleozoic-to-Mesozoic-age central Asian fold belt. The Sino-Korean Craton consists of a series of Archean blocks separated by complex belts of deformed Proterozoic rocks

[*Xu and Ma*, 1992]. Radiometric dating shows the basement rocks are 2.5–3.8 Ga [*Jahn et al.*, 1987; *Song et al.*, 1996], but U-Pb ages of detrital zircons indicate the existence of crustal rocks older than 3.8 Ga [*Liu et al.*, 1992]. The basement rocks of the Sino-Korean Craton are overlain by a thick sequence of Proterozoic and Paleozoic sediments, suggesting that the craton was stabilized by at least the middle Proterozoic. Paleomagnetic studies indicate that the amalgamation of the Siberian Platform and the Sino-Korean Craton started in the Permian (~ 275 Ma) and was completed by the late Jurassic (~ 200 Ma) [*Zhao et al.*, 1990].

[34] The Sino-Korean Craton has a high-velocity lithospheric root extending to ~ 225 km depth beneath the western part of the craton (west of $\sim 110^{\circ}$ E), but the high-velocity root is missing beneath the Archean crust of the eastern part of the craton. (Figures 4 and 8c). This difference between the eastern and western parts of the Sino-Korean Craton has been previously noted [*Menzies et al.*, 1993; *Lebedev and Nolet*, 2003; *Priestley and Debayle*, 2003]. Kimberlitic magmas erupted on the eastern Sino-Korean Craton during the Paleozoic, entraining garnet-diamond facies mantle nodules [*Menzies et al.*, 1993; *Menzies and Xu*, 1998; *Griffin et al.*, 1998], implying that the craton was underlain by a cool, depleted root extending into the diamond stability field (deeper than about 140 km depth). Since the late Mesozoic the eastern portion of the craton has been tectonically active as indicated by the formation of large sedimentary basins and widespread volcanism [*Ma et al.*, 1984; *Liu*, 1987; *Tain et al.*, 1992]. During the Cenozoic, basaltic magmas entraining spinel-facies nodules were erupted on the same part of the craton as the earlier diamond-bearing kimberlites [*Menzies and Xu*, 1998; *Griffin et al.*, 1998; *Xu et al.*, 1998], suggesting that the cool, depleted mantle root beneath the eastern part of the craton had been thinned or replaced by warm, fertile mantle by this time. Presently, the eastern portion of the Sino-Korean Craton has high heat flow [*Ma et al.*, 1984] and extensive seismicity [*Wesnousky et al.*, 1984], indicating a fundamentally different nature of the mantle lithosphere beneath the eastern and western parts of the Sino-Korean Craton that is consistent with the difference in the mantle structure we see in our S_v wave speed model.

[35] To the north of the Sino-Korean Craton lies another high-velocity feature in our S_v model (Figures 4b–4d) which approximately coincides with the Songliao Basin (Figure 1). *Zhang et al.* [1998] analyzed potassic volcanic rocks and mantle xenoliths from the Songliao Basin and concluded that it is an Archean–early Proterozoic mantle terrane; the high-velocity feature in our model to the north of the Sino-Korean Craton may be related to this proposed Archean–early Proterozoic mantle terrane.

[36] The Sichuan Basin forms the Archean core of the Yangtze Craton (Figure 1). An isolated high-velocity feature exists at 100 km depth beneath the Sichuan Basin (Figure 4a), but by 150 km depth the high-velocity region expands beyond the basin to underlie much of the western part of the Yangtze Craton (Figure 4b) and links up to the west with the high velocities at this depth beneath eastern Tibet. The resolution in our model does not permit us to say whether or not these high-velocity features are continuous. The high-velocity root of the Yangtze Craton is also resolved in the surface wave model of *Lebedev and Nolet* [2003], but in their

model, this feature extends somewhat deeper than in ours (Figure 8b).

[37] There is a major negative velocity anomaly beneath SE China and northern Thailand (Figure 4 and 8b) with low wave speeds extending to ~ 250 km depth. The checkerboard test (Figure 9b) suggests the resolution in this part of the model is good even though it is near the edge of the model.

6.3. Hangay Dome–Baikal Rift Region

[38] A prominent low-velocity anomaly extends from the Altai Mountains to the Baikal rift region south of the Siberian Platform (Figure 4). Low velocities in the vicinity of Lake Baikal have been reported in previous surface wave tomography models of Asia. *Curtis et al.* [1998] note low velocities in the Baikal region in their 80 s phase velocity map with the zone of lowest velocity southeast of Lake Baikal; *Villaseñor et al.* [2001] observe a large, low-velocity region beneath Mongolia with its largest anomaly occurring southwest of Lake Baikal; and *Friederich* [2003] found a well-confined, nearly cylindrical low-velocity anomaly beneath the southern tip of the Baikal rift reaching down into the transition zone. At 100 km depth in this part of our model (Figure 4a), there is low-velocity mantle extending as far west as the Altai Mountains, similar to that seen in the shear wave model of *Villaseñor et al.* [2001], but by 150 km depth the mantle beneath the Altai Mountains is relatively fast and the low mantle velocities extend only to as far west as $\sim 100^{\circ}$ E.

[39] The western portion of this low-velocity anomaly occurs beneath the region of the Hangay Dome which forms the large part of the Mongolian Plateau, a 800-km-long N-S topographic bulge characterized by elevations typically exceeding the regional trend of ~ 1.5 km [*Windley and Allen*, 1993] (Figure 1). It is an area of recent uplift, diffused extension, high seismicity, high heat flow, and recent Cenozoic volcanism [*Kiselev*, 1987; *Cunningham*, 1998; *Bayasgalan et al.*, 2005]. Regional heat flow data show the highest values over the Hangay Dome decreasing radially away from the dome [*Cunningham*, 1998]. The timing of Cenozoic uplift is not well constrained [*Cunningham*, 2001], but it appears that most of the present-day topography dates from the Oligocene to early Miocene [*Cunningham*, 2001; *Cunningham et al.*, 1996; *Baljinnyam et al.*, 1993]. These features have been cited as evidence for a juvenile mantle plume or asthenospheric diapir that also extends northeastward beneath Lake Baikal [*Zorin et al.*, 1989; *Kiselev and Popov*, 1992; *Windley and Allen*, 1993] although others argue against the existence of a plume below the Hangay Dome [*Khutorskoy and Yarmoluk*, 1989].

[40] *Villaseñor et al.* [2001] point out that the Hangay Dome coincides with the significant upper mantle low-velocity anomaly WSW of Lake Baikal in their model. However, our model shows that this is not a deep-seated, low-velocity anomaly but west of 100° E it is a shallow feature extending no deeper than ~ 125 km. The Hangay volcanic field (Figure 4) lies above the transition from high to low velocity at deeper depths. Studies of xenoliths from recent (1 Ma) Tariat volcanics [*Ionov et al.*, 1998] indicate that the source of this magmatism is deeper than 70 km. Some mantle xenoliths of the Mongolia lavas have Proterozoic model ages and show evidence of long term (\geq Ga)

depletion in incompatible trace elements, suggesting derivation from old, cold, basalt-depleted lithosphere compatible with the higher velocities seen at deeper depths beneath this region. However, the geotherm for Tariat (Figure 10c) shows very thin lithosphere associated with the Cenozoic volcanism.

[41] Farther east the northern edge of the low-velocity anomaly coincides with the Baikal Rift. The extensional deformation of the rift is thought to result from either far-field effects of the Indo-Eurasian collision [Molnar and Tapponnier, 1975; Tapponnier and Molnar, 1979], from a mantle upwelling beneath rift axis [Logatchev and Zorin, 1987, 1992; Kiselev and Popov, 1992], or a combination of both [Petit et al., 1998]. However, Ionov et al. [1995] showed that the nodules from volcanics near the rift axis are fertile Iherzolite, but equilibration temperatures are no higher than those from volcanics at other locations farther from the rift and all are well below temperatures expected for mantle diapirs. Lowman and Jarvis [1996] show that due to blanketing effects, mantle upwelling can persist for a long time after continental suturing and such upwelling can cause small-scale tensional stresses; Petit et al. [2002] suggest this as a possible explanation for the low velocities seen in the upper mantle and for the extension observed at the surface. However, the suturing of the Siberian Platform and the Sino-Korean Craton was complete by \sim 200 Ma [Zhao et al., 1990]. Whatever the deep-seated cause of the volcanics and rifting, the high-velocity lid we image west and north of the low velocity anomaly and which appears to equate with the cold lithosphere (Figures 8a, 8b, 10a, and 10b) appears to be the controlling factor in the proposed mantle upwelling.

6.4. Indo-Eurasian Collision Zone

[42] For the past \sim 50 Ma Asian tectonics has been dominated by the collision of India and southern Eurasia. The continued northward motion of India since the closure of the Tethys Ocean has uplifted the Himalaya Mountains and the Tibetan Plateau. However, how the collision relates to structures in the upper mantle is still unclear. At shallow depths (<100 km) in our model, India is fast and the Tibetan Plateau is slow with respect to the reference model (Figure 4a); however, by 150 km depth the mantle beneath Tibet is fast (Figure 4b). Figures 8d and 8e show two profiles through the model crossing the Indo-Eurasian collision zone and these show fast Indian mantle dips northward beneath Tibet. At shallower depths beneath Tibet the velocities are low. These low velocities extend to somewhat deeper depths beneath northern Tibet than they do beneath southern Tibet (Figure 8e). An isolated high-velocity anomaly underlies the Tarim Basin at shallow depths (Figure 4a), but by 150 km depth this merges with the high velocities beneath the western Tibetan Plateau (Figure 4b).

[43] Both surface wave group [Ritzwoller and Levshin, 1998] and phase [Curtis et al., 1998; Griot et al., 1998a] velocity tomographic studies of the Tibetan Plateau show a change from low to high velocity with increasing period, consistent with the low velocity at shallow depth and high velocities at deeper depths that we see beneath the plateau. Griot et al. [1998a] suggested that the low phase velocity at short period (<70 s) resulted from the thick crust and possible partial melting in the uppermost mantle litho-

sphere, and the high phase velocity at long-period (>70 s) results from the inward plunge of the cold lithospheric mantle surrounding Tibet. However, more detailed seismic studies show that the low velocities in the uppermost mantle are confined to the northern part of the plateau and that the thickest crust occurs in the southern part of the plateau [Ni and Barazangi, 1983; McNamara et al., 1995; Woodward and Molnar, 1995; McNamara et al., 1997; Yuan et al., 1997; Wittlinger et al., 2004; Rapine et al., 2003; Mitra et al., 2005]. Therefore the pattern of low velocity we see at shallow depths beneath Tibet (Figures 8d and 8e) is not likely to result solely from the thick Tibetan crust.

[44] On the basis of the low uppermost mantle velocity seen beneath northern Tibet coupled with the nature of the volcanics on the northern part of the plateau [Chung et al., 2005], a model for plateau uplift involving lithospheric delamination has been proposed [Molnar, 1988; Molnar et al., 1993]. However, our mantle model (Figures 8d and 8e) shows that high-velocity material underlies most and possibly all of Tibet to a depth of 225–250 km. This suggests that the Indian lithosphere has not detached and sunk beneath the plateau but that most of the plateau has been underthrust by high-velocity Indian mantle from the south and possibly to a lesser extent, high-velocity Asian mantle from the north. However, because of the smoothing due to the long wavelengths of our surface wave data and the 400 km correlation length used in the tomographic inversion, we cannot rule out a narrow upwelling beneath the plateau as proposed by Tilman et al. [2003]. McNamara et al. [1995] found that whereas S_n from near events was blocked for paths crossing the northern part of the plateau, S waves from events at larger regional distances did propagate efficiently beneath the plateau, supporting the continuity of the high velocity lid beneath most, if not all, of Tibet.

[45] There are two intriguing features deeper in the mantle beneath India and Tibet. By 250 km depth the high-velocity mantle beneath Peninsular India and northern Tibet has largely disappeared, but high velocities persist beneath the Himalaya and southern Tibet and extend to the southeast beneath northern Burma (Figure 4d), a region of deep seismicity. Profile EE' (Figure 8e) shows that this is a high-velocity tabular feature extending to the base of our model and suggests that India has overridden a subducted lithospheric fragment. High velocities beneath southern Tibet have been noted in past body wave studies [Pandey et al., 1991; Zhou et al., 1996; Tilman et al., 2003]. Tilman et al. [2003] invert P wave traveltimes residual from INDEPTH II and III data and found a high velocity structure extending to \sim 400 km depth beneath southern Tibet. They discount that this high-velocity anomaly is a remnant of the Tethys Oceanic lithosphere as observed deeper in the mantle to the south beneath India [Van der Voo et al., 1999] because such a body of dense and cold material would not be stable over 50–60 Ma and would have sunk into the mantle or been thermally eroded. Instead Tilman et al. [2003] suggest this is delaminated Indian continental lithosphere as proposed by Chemenda et al. [2000]. However, the Chemenda et al. [2000] model depends on India having a weak lower crust and it is becoming increasingly clear that this is not the case [Jackson, 2002; Jackson et al., 2004]. In addition, the Precambrian crust of the Indian subcontinent today is underlain by a

fast, buoyant root, similar to but somewhat thinner than the other shields and such buoyant material would not delaminate and sink. On the other hand, there are fragments of oceanic lithosphere such as the Black Sea and the Caspian Sea, presently caught up in other parts of the Alpine-Himalayan belt. These persist for a time but will eventually subduct, forming an intermediate-depth, dipping seismic zone within the continental interior, such as that presently observed below the Hindu Kush [Priestley et al., 1994; Jackson et al., 2002]. The high-velocity, steeply dipping slab (Figures 8d and 8e) beneath southern Tibet may result from a similar process.

[46] Finally, there is a low-velocity feature extending to the base of the model beneath Gujarat India (Figures 4 and 8e), but this is near the edge of our model and we have less confidence in the resolution of this feature than in the resolution of features farther north in the model. This low-velocity anomaly is small in size in the upper parts of the model but broadens with depth. *Kennett and Widjiantoro* [1999] noted a similar feature in their P wave tomographic model.

6.5. Subduction Zones and Back-Arc Basins

[47] The subduction zones and back-arc basins of the northwest Pacific have been imaged in numerous body wave tomographic models [e.g., *van der Hilst* et al., 1993] and are not the focus of this paper. However, they do provide insight into the resolution of our S_V model. The thickness of the old oceanic lithosphere being subducted beneath Japan is ~ 100 km [McKenzie et al., 2005], whereas the thickness of the subducting oceanic lithosphere imaged in the model is 400–500 km, yielding a qualitative estimate of the model resolution, at least in this part of the model. The NW Pacific back-arc basins from the northern part of the South China Sea to the Sea of Okhotsk have low-velocity structures extending to 200–250 km depth with wave speeds at 100–150 km depth $\sim 8\%$ slow with respect to the reference model (Figures 4, 8a, and 8c).

7. Anisotropy

[48] The pattern of azimuthal anisotropy in our model is complex at shallow depths and decreases in both amplitude and complexity with increasing depth (Figure 4). Much of the shallow azimuthal anisotropy is likely to be inherited from past episodes of orogenic deformation and the superposition of a number of such episodes on the continents can result in an anisotropic fabric that varies over a smaller length scale than that in the ocean where the plate formation and asthenospheric flow patterns are much simpler. The azimuthal anisotropy resolution test discussed above shows that the recovered azimuthal anisotropy by our surface wave analysis may be unreliable in regions where the pattern of azimuthal anisotropy changes rapidly with respect to the wavelength of the surface waves.

[49] *Griot* et al. [1998b] measured phase velocity for 619 vertical and 254 horizontal component seismograms for paths crossing eastern China and Tibet with the highest path density in eastern China. Their tomographic technique is similar to that applied in our study, but they provide no resolution tests for azimuthal anisotropy. They observed strong lateral variations in azimuthal anisotropy over rela-

tively narrow zones beneath Tibet and conclude that down to 200 km depth the observed pattern of azimuthal anisotropy reflected a deformation coherent with the motion on a small number of major faults extending deep into or through the lithosphere. Our path density and azimuthal coverage of Tibet are substantially better than that of *Griot* et al. [1998b] and while our azimuthal anisotropy observations are broadly in agreement with theirs, the resolution tests presented in this study call into question the conclusions of *Griot* et al. [1998b] concerning the pattern of the azimuthal anisotropy.

[50] Laboratory experiments on olivine aggregates suggest that at deeper depths in the mantle, flow orients crystals and results in a lattice-preferred orientation (LPO) which gives rise to azimuthal anisotropy for seismic wave propagation. The degree of alignment of olivine crystals is believed to be strain-dependent. Simple shear at the base of a moving plate will produce anisotropy with a fast a axis that follows the principal extension direction for moderate deformation and aligns with the flow direction for large deformation [Zhang and Karato, 1995]. There are a range of situations where complications can occur. *Kaminski* and *Ribe* [2002] show that there is a timescale for crystal alignment along the flow. When the flow changes abruptly or is disrupted, the fast a axis may not have enough time to follow the rapid change and to align with the flow. Under water-rich conditions, the relations between anisotropy and flow are also complicated [Jung and Karato, 2001]. Although such conditions may not be common in the upper mantle [Kaminski, 2002] they are plausible in subduction zones or in regions where upwelling material contains a large amount of water [Jung and Karato, 2001]. If we assume a relatively water-poor olivine, modest simple shear will produce LPO with a plunging a axis. If the upper mantle anisotropy does result primarily from the preferred alignment of olivine crystals, the direction of fast S_V wave propagation is expected to be along the projection in the horizontal plane of the fast a axis [Lévéque et al., 1998] so the strength of the azimuthal anisotropy will gradually reduce as the a axis departs from the horizontal. Therefore the slow horizontal motion of the Eurasian plate would be expected to produce small basal shear and weak azimuthal anisotropy as is observed below ~ 200 km depth (Figure 4). In fact, *Debayle* et al. [2005] suggest from a global study of azimuthal anisotropy that the Australian plate is the only continental plate moving fast enough to produce large-scale basal shear and large amplitude azimuthal anisotropy. An increase in the amount of clinopyroxene relative to olivine [Beghein and Trampert, 2003] or the activation of a different slip system by high-pressure dislocation creep [Mainprice et al., 2005] may also contribute to reduce the strength of azimuthal anisotropy below 220 km depth.

8. East Asian Lithosphere

[51] The high wave speed roots of the east Asian cratons do not extend deeper than 200–225 km (Figure 4). Nodules from the kimberlite eruptions show that the cratonic root consists of depleted harzburgite with a density that is about 40 kg m^{-3} less than fertile mantle consisting of lherzolite. *Jordan* [1979] shows that the seismic velocity change associated with the depletion is only 0.03 km s^{-1} and *Priestley* and *McKenzie* [2006] show the removal of 25%

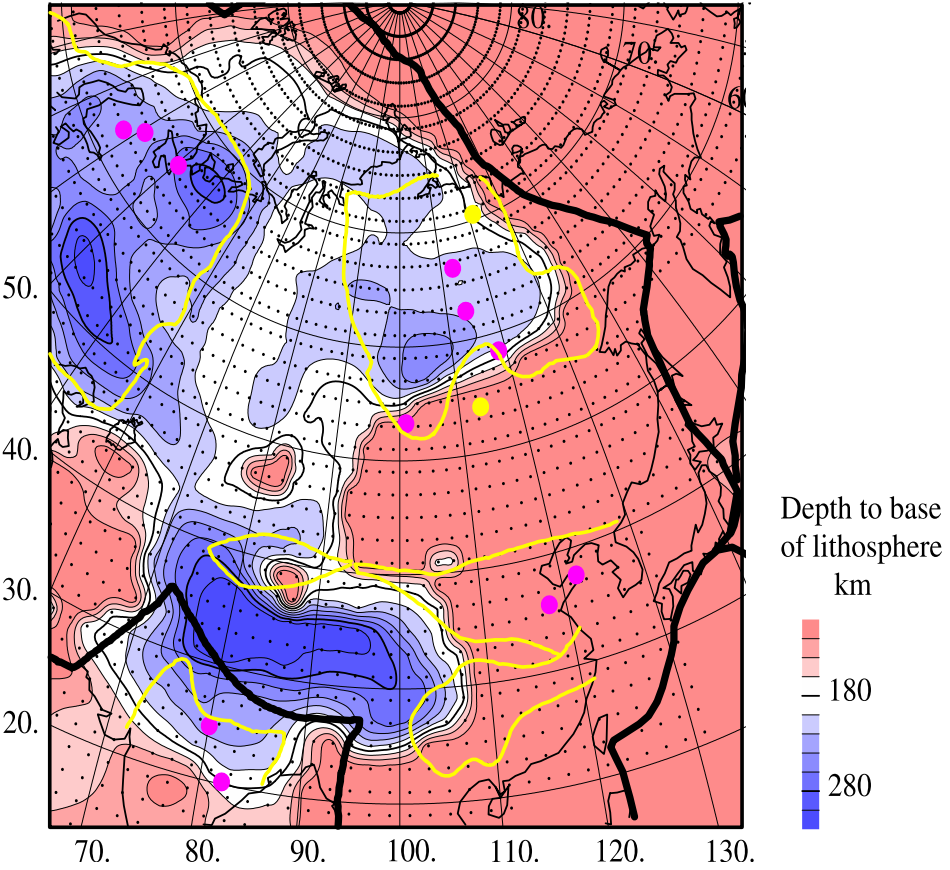


Figure 11. Contours of the thickness of that part of the Asian lithosphere in the diamond stability field calculated from the S_v wave speed Asia model. The small black dots show the locations at which the lithospheric thickness was calculated. The color circles show the locations of kimberlite volcanics (red, diamondiferous; yellow, nondiamondiferous). Yellow lines denote the same tectonic features shown in Figure 1; bold black lines denote plate boundaries.

melt results in a V_s change equivalent to a change in temperature of 96°C when the temperature is less than about 1100° . *McKenzie et al.* [2005] suggest that the mechanical behavior of both the oceanic and continental mantle depends primarily on temperature and *Priestley and McKenzie* [2006] used the correspondence between the V_s and thermal structure of the Pacific plate [*McKenzie et al.*, 2005] to obtain an empirical relationship between the temperature (Θ) in $^\circ\text{C}$, wave speed (V_s), and depth (z). They showed that

$$\begin{aligned} V_s^* &= V_s / (1 + b_V(z - 50)) \\ V_s^* &= m\Theta + c + A \exp(-(E + PV_a)/RT) \end{aligned} \quad (1)$$

where E is the activation energy, V_a the activation volume, T the temperature in $^\circ\text{K}$, and the constant values

$$b_V = 3.84 \times 10^{-4} \text{ km}^{-1}, \quad m = -2.8 \times 10^{-4} \text{ km s}^{-1} \text{ }^\circ\text{C}^{-1},$$

$$c = 4.72 \text{ km s}^{-1}, \quad A = -1.8 \times 10^{13} \text{ km s}^{-1},$$

$$E = 409 \text{ kJ mol}^{-1}, \quad V_a = 10 \times 10^{-6} \text{ m}^3 \text{ mol}^{-1} (\equiv 10 \text{ cm}^3 \text{ mol}^{-1})$$

provide a good fit of $V_s(T)$ for the Pacific lithosphere. Equation (1) can be inverted to obtain $T(z)$ from the values of $V_s(z)$ of Figure 4. Figure 11 shows the variation in the thickness of the thermal lithosphere for eastern Asia derived from the V_s model. Partly because velocities at depths of less than 100 km may be affected by the leakage from the thick low-velocity crust in central Asia, and partly because the temperature estimates are more accurate at high temperature, only those values of $T(z)$ that exceed 1100°C at a depth of 125 km or more were used to obtain the geotherms and to estimate the lithospheric thickness. Estimates of lithospheric thickness from V_s and from the nodule mineralogy are independent and agree to within 20 km [*Priestley and McKenzie*, 2006]. *Priestley and McKenzie* [2006] refer to the low-temperature continental roots as continental “cores.”

[52] The north Eurasian core (Figure 11) consists of the Siberian Platform, the West Siberian Basin and the European Platform. This structure is what we refer to above as stable Eurasia and it is this structure which appears to control the deformation associated with central and southern Asia. This is clear in the Baikal region where the earthquakes of the northeast part of the rift follow the boundary defined by the lithospheric root and not the mapped surface

position of the craton. Other features in Asia with thick thermal lithosphere are the Hindu Kush zone, the Tarim Basin, the western part of the Sino-Korean Craton, the Sichuan Basin, and the northern India–southern Tibet region. The lithosphere is thin beneath the Indian Peninsula and beneath eastern China.

[53] Diamondiferous kimberlites occur on both the east Sino-Korean Craton and the Indian Peninsula (Figure 11). The diamond-bearing kimberlites in eastern China are Ordovician (~475 Ma) age, indicating that the eastern part of the Sino-Korean Craton had a thermal lithosphere extending into the diamond stability field at the time of the kimberlite eruptions, but there is no indication of a cratonic root at present. How such a low-density, buoyant lithosphere could be destroyed is puzzling. It would not be expected to founder because the depleted harzburgite forming the lithosphere is lighter than the underlying fertile mantle; a rise in temperature would also increase its buoyancy. On the other hand, the continental cores are only visible in Figure 11 because their average velocity is high. Perhaps the extension which eastern China has experienced since the Mesozoic has led to a thinning of the depleted root or the root has been intruded by more fertile mantle material associated with the Cenozoic volcanics in eastern China. In these cases the depleted root might be too thin or have an average velocity too low to be resolved by the low-frequency surface waves. Perhaps the cratons of southern India have undergone a similar stretching episode during the disruption of Gondwanaland which may explain why India’s high-velocity cratonic root, while present in our S_v maps, does not extend to as great a depth as do most other cratonic roots.

9. Summary

[54] We have applied multimode surface wave tomography to determine the S_v structure of the Asian upper mantle. The relatively short paths (≤ 6000 km) and dense higher-mode coverage have enabled us to build an upper mantle model for Asia with a horizontal resolution of a few hundred kilometers extending to a depth of ~400 km. At shallow depths (<150 km) in the model there is approximately $\pm 9\%$ S_v wave speed heterogeneity, the amplitude of the azimuthal anisotropy is large, and the pattern of azimuthal anisotropy is complex. At deeper depths (>250 km) the S_v wave speed heterogeneity reduces to approximately ± 2 – 3% , the amplitude of the azimuthal anisotropy decreases, and its pattern becomes less complex. Above ~200 km depth the upper mantle structure of the model is correlated with surface geology and tectonics; below ~200 km depth the structures primarily reflect the advection of material in the upper mantle, primarily the subducting slabs.

[55] The Siberian Platform has a high-velocity root extending to 200–225 km depth whose eastern boundary closely matches the geologically mapped boundary of the platform along the western boundary of the Verkhoyansk fold and thrust belt, but in the west the high-velocity upper mantle lid extends across the West Siberian Basin as far as the Ural Mountains where it merges with the high-velocity root beneath the East European Platform. A prominent low-velocity anomaly extends along the southern boundary of the Siberian Platform beneath the Hangay Dome–Baikal

Rift region. The relationship between the fold-and-thrust belts and the Baikal Rift to the east and south of the platform with the subsurface location of the platform boundary suggests that the thick high wave speed root of the platform is the controlling factor in the deformation of northeastern Asia.

[56] The western part of the Sino-Korean Craton has a high-velocity lithospheric root extending to ~225 km depth, but the high-velocity root is missing or highly attenuated beneath the Archean crust of the eastern part of the craton. This observation is consistent with the petrologic studies which show that diamondiferous kimberlites erupted on the eastern part of the Sino-Korean Craton in the Paleozoic, implying the Archean crust was underlain at that time by a cool, depleted root extending into the diamond stability field. However, in the same region, basaltic magmas entraining spinel-facies nodules were erupted in the Cenozoic showing the lack of such a cool, depleted root at that time. An isolated high-velocity feature exists at 100 km depth beneath the Yangtze Craton, but by 150 km depth the root expands to the west, merging with the high velocities at this depth beneath eastern Tibet.

[57] In our upper mantle model all of Tibet is underlain by high velocity material to a depth of 225–250 km. However, because of the smoothing of the surface waves, we cannot rule out a narrow upwelling beneath the plateau as proposed by Tilman et al. [2003]. High-velocity material occurs to at least 400 km depth beneath southern Tibet and northern India.

[58] We use our S_v wave speed upper mantle model and the results of Priestley and McKenzie [2006] to produce a contour map of the thermal lithospheric thickness of eastern Asia. Our lithospheric model shows an extensive region of thick lithosphere beneath the Siberian Platform and the West Siberian Basin that extends west to the European Platform, forming the stable Eurasian craton or core. The eastern portion of this structure appears to be controlling the geometry of continental deformation in this region. Thick, cold lithosphere also underlies Tibet and the Tarim Basin but is absent from beneath the Indian shield and the eastern Sino-Korean craton.

[59] **Acknowledgments.** This study would not have been possible without permanent and temporary seismographs operated in Asia, Europe, and North America. Our study has included data from the ASRO/SRO, CDSN, CNSN, ERI/STA, GEOFON, GEOSCOPE, IRIS-IDA, IRIS-USGS, KNET, and KZNET permanent seismic networks and the Tibetan Plateau Broadband Experiment, Kamchatka Subduction Zone, INDEPTH II, INDEPTH III, and GHENGIS PASSCAL temporary seismic deployments. This research has benefited from discussions with M. Cara, J. Jackson, J.-J. Leveque, and F. Tilman. Priestley would like to thank both the Institut de Physique du Globe de Strasbourg and GeoForschungsZentrum, Potsdam, for supporting time to pursue this work. Debayle was supported by programme DyETI conducted by the French Institut National des Sciences de l’Univers (INSU). A number of the figures were prepared using Generic Mapping Tool [Wessel and Smith, 1995]. This is Cambridge University Department of Earth Sciences contribution ES8481.

References

- Artemieva, I., and W. Mooney (2001), Thermal thickness and evolution of precambrian lithosphere: A global study, *J. Geophys. Res.*, 106, 16,387–16,414.
- Baljinnyam, I., et al. (1993), Ruptures of major earthquakes and active deformation in Mongolia and its surroundings, *Mem. Geol. Soc. Am.*, 181, 1–59.
- Bayasgalan, A., J. Jackson, and D. McKenzie (2005), Lithosphere rheology and active tectonics in Mongolia: Relations between earthquake source

- ringwoodite to 20 GPa and 1373 K, *Phys. Earth Planet. Inter.*, **143**, 321–336, doi:10.1016/j.pepi.2004.03.005.
- Yin, A., and S. Nie (1996), A phanerozoic palinspastic reconstruction of China and its neighboring regions, in *The Tectonic Evolution of Asia*, edited by A. Yin and T. Harrison, pp. 442–485, Cambridge Univ. Press, New York.
- Yoshizawa, K., and B. Kennett (2002), Determination of the influence zone for surface wave paths, *Geophys. J. Int.*, **149**, 440–453.
- Yuan, X., J. Ni, R. Kind, J. Mechie, and E. Sandvol (1997), Lithospheric and upper mantle structure of southern Tibet from a seismological passive source experiment, *J. Geophys. Res.*, **102**, 27,491–27,500.
- Zhang, M., X.-H. Zhou, and J.-B. Zhang (1998), Nature of the lithospheric mantle beneath NE China: Evidence from potassio volcanic rocks and mantle xenoliths, in *Mantle Dynamics and Plate Interaction in East Asia*, *Geodyn. Ser.*, vol. 27, edited by M. Flower, pp. 197–219, AGU, Washington, D. C.
- Zhang, S., and S. Karato (1995), Lattice preferred orientation of olivine aggregate deformed in simple shear, *Nature*, **375**, 774–777.
- Zhao, X., R. Coe, Y. Zhou, H. Wu, and J. Wang (1990), New paleomagnetic results from northern China: Collision and suturing with Siberia and Kazakhstan, *Tectonophysics*, **181**, 43–81.
- Zhou, R., S. Grand, F. Tajima, and X. Ding (1996), High velocity zone beneath the southern Tibetan Plateau from P-wave differential travel-time data, *Geophys. Res.*, **23**.
- Zolutkin, V., and A. Al'mukhamedov (1988), Traps of the Siberian Platform, in *Continental Flood Basalts*, edited by J. Macdougall, pp. 272–310, Springer, New York.
- Zorin, Y., V. Kozhevnikov, M. Novoselova, and E. Turutanov (1989), Thickness of the lithosphere beneath the Baikal rift zone and adjacent regions, *Tectonophysics*, **168**, 327–337.

E. Debayle, Ecole et Observatoire des Sciences de la Terre, CNRS and Université Louis Pasteur, F-67084 Strasbourg, France. (eric.debayle@eost.u-strasbg.fr)

D. McKenzie, S. Pilidou, and K. Priestley, Bullard Laboratories, Madingley Rise, Madingley Road, Cambridge, CB3 0EZ, UK. (mckenzie@esc.cam.ac.uk; pilidou@esc.cam.ac.uk; keith@madingley.org)